



## 28 **1. Introduction**

29 Terrestrial ecosystem evapotranspiration (E) is the primary pathway by which land surface  
30 moisture returns to the atmosphere and thus plays a central role in the global water cycle (Liu et al.,  
31 2023; Sun et al., 2022). E comprises three components: soil evaporation (Es), vegetation canopy  
32 interception (Ei), and plant transpiration (T) (Niu et al., 2020; Wei et al., 2017). Among these,  
33 vegetation transpiration, by which water is released to the atmosphere through plant stomata,  
34 accounts for over 60% of total terrestrial E (Li et al., 2024; Wei et al., 2017). As transpiration is  
35 closely linked to carbon assimilation and energy exchange, the vegetation transpiration fraction (TF,  
36 defined as  $T/E$ ) quantifies the contribution of vegetation to land–atmosphere water–vapor flux and  
37 is a key indicator of vegetation–climate coupling strength (Schlesinger and Jasechko, 2014; Wei et  
38 al., 2017). Understanding changes in TF is crucial for revealing ecohydrological mechanisms and  
39 accurately predicting climate–change impacts.

40 Persistent climate warming and rising atmospheric CO<sub>2</sub> over the past few decades have driven  
41 global vegetation greening and altered ecosystem water balances (Denissen et al., 2022; Hu et al.,  
42 2023). Increases in Leaf area index (LAI) directly enhance canopy interception and transpiration  
43 potential; global plant transpiration is estimated to have increased by about 6% from 1990–2020,  
44 primarily as a consequence of increased LAI (Chen et al., 2024). However, the positive effect of  
45 LAI on transpiration depends on water availability: when soil moisture (SM) is scarce or  
46 atmospheric drought, often represented by vapor pressure deficit (VPD), intensifies, plants close  
47 their stomata to suppress water loss, thereby reducing both transpiration and photosynthesis (Liu et  
48 al., 2020b; Zahra et al., 2023). SM represents the supply-side constraint, whereas VPD represents  
49 the atmospheric demand-side pull; these two factors often co-vary and can together impose  
50 compound drought stress on ecosystems (Song et al., 2024). High VPD induces partial stomatal  
51 closure to prevent excessive water loss and hydraulic failure, causing transpiration rates per unit  
52 leaf area to saturate or even decline under very high VPD conditions (Grossiord et al., 2020; Novick  
53 et al., 2016). Therefore, even as LAI increases, the additional leaf area struggles to further increase  
54 T under extreme atmospheric drought (Xu et al., 2023). Conversely, under moderate SM and  
55 appreciable atmospheric demand, vegetation can maintain both water supply and evaporative  
56 demand at levels that support transpiration, allowing increases in LAI to exert a stronger positive

57 effect on TF (Liu et al., 2020a). During extreme soil drought, increased surface sensible heat further  
58 dries the near-surface atmosphere, creating positive SM–VPD feedback that exacerbates drought  
59 conditions (Qing et al., 2022; Zhou et al., 2019). Accurately characterizing the response of TF to  
60 changes in LAI therefore requires a unified framework that accounts for the synergistic and  
61 nonlinear effects of both soil water supply and atmospheric demand (Koehler et al., 2023). In recent  
62 years, discrepancies have emerged regarding the relative roles of SM and VPD: some studies have  
63 emphasized that atmospheric drought imposes greater limits on ecosystem water–carbon cycles  
64 (Novick et al., 2016), whereas others, after decoupling the coupled effects of VPD and SM, have  
65 found that soil moisture is the dominant factor, especially in semi-arid regions, where SM typically  
66 imposes a stronger limitation on productivity (Liu et al., 2020a). Because SM and VPD are often  
67 strongly correlated, quantifying their relative roles under coupled hydroclimatic conditions remains  
68 a central challenge in ecohydrological research.

69 Since the 1970s, China has implemented some of the world’s largest-scale afforestation and  
70 ecological restoration programs, increasing forest cover from approximately 12% in the 1970s to  
71 over 22% in recent years (Cheng et al., 2025). China’s forests now comprise extensive natural and  
72 planted forests. Natural forests are concentrated mainly in the mountainous regions of northeastern  
73 and southwestern China, whereas planted forests are more widespread in eastern, central, and  
74 southern China (Cheng et al., 2024b). Compared with natural forests, planted forests in China are  
75 more often younger, structurally simpler, and dominated by single-species or even-aged stands  
76 under more intensive management (Cheng et al., 2024a; Farooq et al., 2021). These differences in  
77 origin, structure, and water-use strategies may underlie substantial disparities between NF and PF  
78 in soil water acquisition, stomatal regulation, and hydraulic safety margins, thereby leading to  
79 different responses of TF to changes in LAI (hereafter, LAI–TF sensitivity, denoted as  $\theta$ ). Exploring  
80 these disparities between forest types can deepen the understanding of vegetation water-use  
81 mechanisms and improve regional water-resource management, afforestation benefit assessment,  
82 and climate-adaptive forestry strategies. However, systematic research on this issue is currently  
83 lacking. Existing studies have mostly examined the sensitivity of transpiration or productivity to  
84 drought stress at global or broad regional scales (Liu et al., 2020a; Novick et al., 2016), or have  
85 focused on ecohydrological processes in specific arid regions, without a comparative assessment of

86  $\theta$  across forest types along a unified climatic gradient. This raises four interrelated questions: (1)  
87 Are there systematic differences in  $\theta$  between NF and PF along the climatic gradient from humid to  
88 semi-arid conditions? (2) How have these differences changed over the last 30 years? (3) Under  
89 coupled changes in SM and VPD, what are the relative roles of these two factors in shaping  $\theta$ , and  
90 do these roles vary across climatic backgrounds or over time? (4) Through which hydrological  
91 pathways (SM and/or VPD) do changes in macroclimate, such as radiation, precipitation,  
92 temperature, and wind speed, indirectly affect  $\theta$ ? Addressing these questions will help fill important  
93 research gaps and deepen our understanding of forest–water relations under climate change.

94 The objectives of this study were to quantify the spatiotemporal patterns of transpiration  
95 sensitivity ( $\theta$ ) in China’s natural forests (NF) and plantation forests (PF) from 1990 to 2020 and to  
96 identify the hydroclimatic controls underlying these patterns. To this end, we integrated multi-  
97 source remote-sensing and reanalysis data to derive growing-season LAI, evapotranspiration  
98 components, and meteorological variables for forest pixels at 0.1° resolution. We first used the  
99 aridity index (AI) framework to characterize the climatic background across four climatic zones and  
100 then focused the statistical analyses on the humid, semi-humid, and semi-arid zones to ensure  
101 comparability. We then applied complementary analytical approaches at different statistical scales:  
102 pooled spatial binning was used to characterize the response surface of  $\theta$  along the joint SM–VPD  
103 gradient and to compare spatial contrasts under comparable hydroclimatic backgrounds, whereas  
104 sliding-window partial correlation and ridge regression were used to quantify the independent  
105 temporal associations of SM and VPD with  $\theta$  and their evolution over time. Finally, pathway  
106 analysis was used to decompose the indirect effects of macroclimate change on  $\theta$  through local  
107 hydrological pathways. All trends were estimated using the Theil–Sen slope and evaluated with the  
108 Mann–Kendall test. We further assessed robustness through cross-product comparison and  
109 examined whether atmospheric CO<sub>2</sub> and stand age altered the main interpretation. Together, this  
110 framework was designed to reveal both the spatial heterogeneity and temporal evolution of  
111 hydroclimatic controls on  $\theta$  in China’s contrasting forest types.

## 112 **2. Materials and methods**

### 113 **2.1. Data**

114 We used datasets describing forest type, canopy structure, evapotranspiration components,

115 hydroclimate, and several auxiliary background factors (Table 1). Forest type data were obtained  
116 from the 1990–2020 spatial distribution dataset of natural and plantation forests in China (Cheng et  
117 al., 2024b). This dataset was derived from Landsat imagery and extensive forest inventory samples  
118 using machine-learning classification and was resampled to 0.1° resolution to match the  
119 hydroclimatic datasets. Pixels with 100% coverage of either natural forest (NF) or plantation forest  
120 (PF) were treated as pure pixels, and only these pixels were included in all major analyses. To  
121 maintain temporal consistency between forest masks and climate data, we adopted a period-based  
122 dynamic matching strategy. Specifically, forest maps for 1990, 1995, 2000, 2005, 2010, 2015, and  
123 2020 were used to represent the periods 1990–1994, 1995–1999, 2000–2004, 2005–2009, 2010–  
124 2014, 2015–2019, and 2020, respectively.

125 LAI was derived from the GIMMS LAI4g dataset (Cao et al., 2023). The main  
126 evapotranspiration dataset used in this study was GLEAM v4.2a, from which transpiration (T),  
127 evapotranspiration (E), and soil moisture (SM) were extracted. GLEAM separately estimates the  
128 major components of terrestrial evaporation and provides both surface and root-zone soil moisture.  
129 In this study, SM refers to the root-zone soil moisture product, rather than surface soil moisture,  
130 because it more closely represents plant-available water relevant to transpiration regulation at the  
131 seasonal to interannual scales considered here. In GLEAM, root-zone soil moisture is represented  
132 as a vegetation-accessible multi-layer soil profile constrained by assimilated surface observations,  
133 rather than as a single shallow soil layer. Near-surface meteorological variables, including air  
134 pressure (Pa), relative humidity (RH), air temperature (Ta), precipitation (P), dewpoint temperature  
135 (Td), wind speed (WS), net radiation (Rn), and potential evapotranspiration (PET), were obtained  
136 from ERA5-Land. All environmental variables were aggregated over the growing season (April–  
137 October) for 1990–2020, using only growing-season data and excluding non-growing-season  
138 observations. Means were used for state variables (e.g., LAI, SM, Ta, and VPD), whereas  
139 cumulative values were used for flux variables (e.g., E, T, and P).

140 To evaluate the robustness of the estimated  $\theta$  patterns and trends to data-product choice, we  
141 additionally used two alternative gridded products for cross-product comparison in supplementary  
142 analyses. One was the Simple Terrestrial Hydrosphere v2 (SiTHv2) product, which provides  
143 independent estimates of evapotranspiration and transpiration (Zhang et al., 2024). The other was

144 the China terrestrial ecosystem transpiration fraction dataset (Niu et al., 2020), from which an  
 145 alternative transpiration-fraction-based  $\theta$  estimate was derived for comparison. These two datasets  
 146 were used only for robustness assessment of  $\theta$ , whereas all main calculations in the study were based  
 147 on GLEAM.

148 To assess whether long-term changes in  $\theta$  may also be modulated by non-hydroclimatic  
 149 background factors, we further compiled several auxiliary datasets for supplementary analyses,  
 150 including a global 1-km atmospheric carbon dioxide concentration dataset (Wang, 2026), a long-  
 151 term reconstructed forest age dataset for China (Xia et al., 2023), and a 2020 forest age spatial  
 152 distribution dataset for China (Cheng et al., 2024a). These auxiliary datasets were resampled to  $0.1^\circ$   
 153 resolution and used only to assess whether  $\text{CO}_2$  and stand age materially altered the observed  $\theta$   
 154 patterns and trends. They were not included in the main analytical framework, in which the focus  
 155 was on hydroclimatic controls.

156 **Table 1. Data overview**

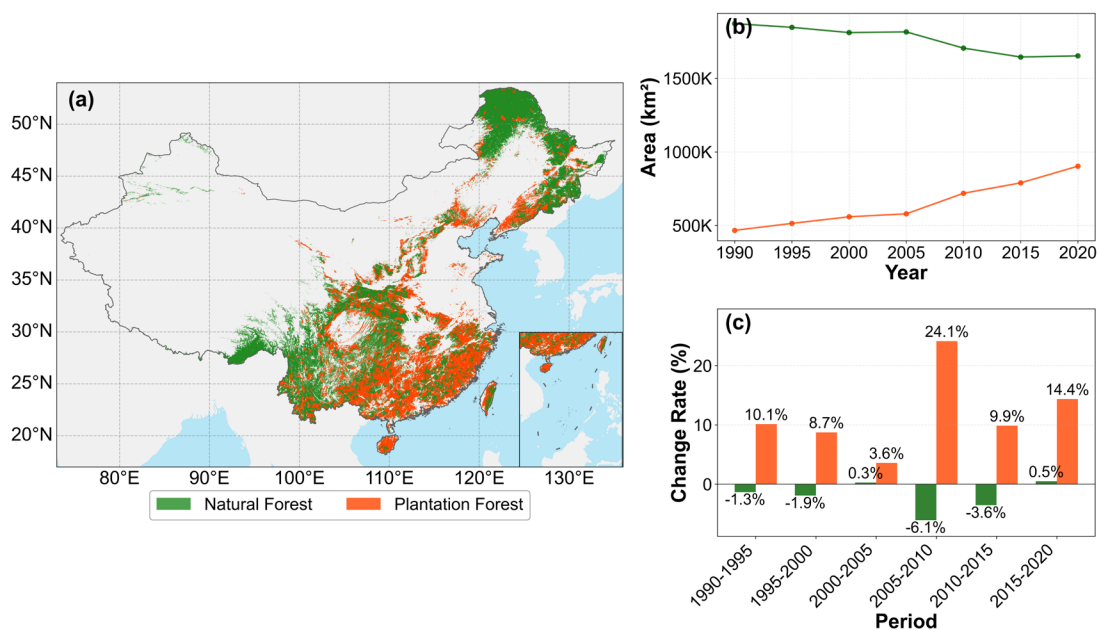
Variable	Data set	Resolution (spatial)	Resolution (temporal)	Time span	References
Forest type	Planted and natural forest maps in China from 1990 to 2020	1 km	5 years	1990– 2020	Cheng et al., 2024b
LAI	GIMMS LAI4g	$1/12^\circ$	15 day	1982– 2020	Cao et al., 2023
E, T, SM	GLEAM v4.2a	$0.1^\circ$	1 day	1980– 2023	Miralles et al., 2025
Validation data	SiTHv2	$0.1^\circ$	1 day	1982– 2020	Zhang et al., 2024
	China terrestrial ecosystem transpiration fraction dataset	$0.05^\circ$	8 day	1981– 2015	Niu et al., 2020
Ta, Pa, RH, Td, P, PET, Rn, WS	ERA5-Land	$0.1^\circ$	1 month	1950– 2025	Muñoz-Sabater et al., 2021
CO <sub>2</sub>	Global 1 km atmospheric carbon dioxide concentration dataset	1 km	annually	2003– 2023	Wang, 2026
forest age	Long-term reconstructed forest age dataset for China	1 km	annually	1980– 2015	Xia et al., 2023
	2020 forest age spatial distribution dataset for China	30 m	static	2020	Cheng et al., 2024a

157 LAI, Leaf area index; E, Evapotranspiration; T, Transpiration; SM, Root-zone soil moisture; Ta,

158 Air temperature; Td, Dewpoint temperature; Pa, Air pressure; P, Precipitation; PET, Potential  
 159 evapotranspiration; Rn, Net radiation; WS, wind speed.

## 160 2.2. Study region

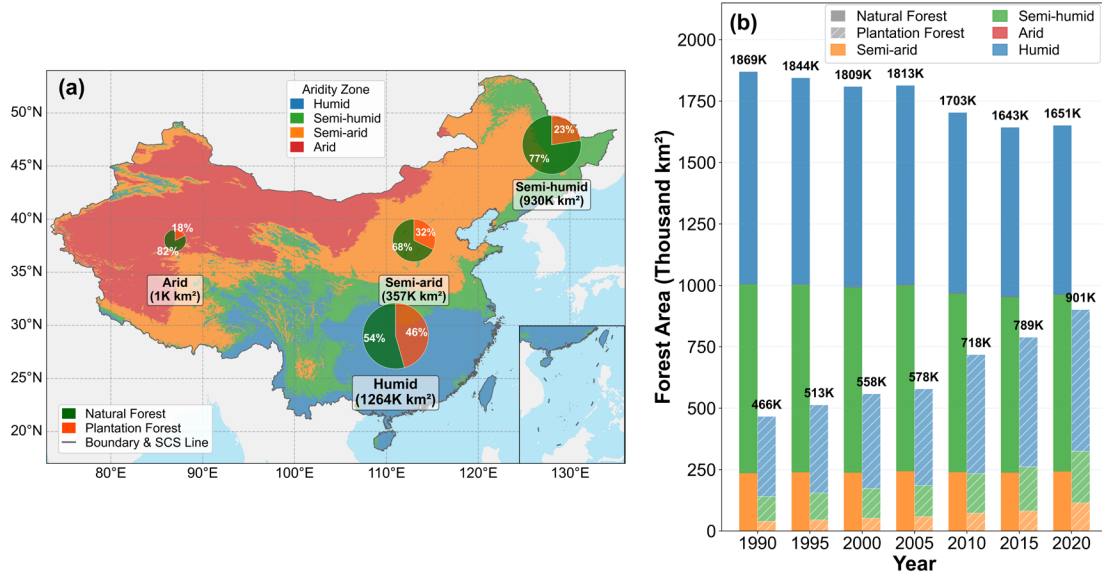
161 Our study area covers terrestrial China, spanning temperate, subtropical, and tropical climate  
 162 zones. The analysis focuses on China's NF and PF. NF are mainly concentrated in the mountains of  
 163 Northeast and Southwest China, whereas PF are widely distributed across the plains and hills of  
 164 East, Central, and South China (Figure 1a). The vast majority of NF and PF are located in humid  
 165 and semi-humid zones (Figure 2).



166  
 167 **Figure 1. Spatiotemporal characteristics of China's natural forests (NF) and plantation forests**  
 168 **(PF) from 1990 to 2020.** (a) Average spatial distribution of NF (green) and PF (orange) in China  
 169 from 1990 to 2020. (b) Dynamic changes in the area (km<sup>2</sup>) of NF and PF from 1990 to 2020. (c)  
 170 Rate of change (%) in NF and PF area for each five-year period from 1990–2020.

171 We used the aridity index (AI) to characterize climatic background and to organize the spatial  
 172 analyses within a unified framework. AI was defined as the ratio of annual potential  
 173 evapotranspiration to annual precipitation ( $AI = PET / P$ ). Based on the 1990–2020 multi-year mean  
 174 AI, China was divided into four climatic zones: humid ( $AI < 1$ ), semi-humid ( $1 \leq AI < 1.5$ ), semi-  
 175 arid ( $1.5 \leq AI < 4$ ), and arid ( $AI \geq 4$ ). This four-zone classification was used as the geographic  
 176 framework for mapping and descriptive comparisons. Because forest samples in the arid zone were

177 extremely sparse, subsequent statistical analyses were restricted to the humid, semi-humid, and  
 178 semi-arid zones.



179  
 180 **Figure 2. Spatiotemporal distribution and composition of forests in different climatic zones in**  
 181 **China from 1990 to 2020.** (a) Spatial distribution of the four climatic zones (humid, semi-humid,  
 182 semi-arid, and arid) in China; the pie charts show the total forest area within each zone and its  
 183 composition of natural forest (green) and planted forest (orange). (b) Dynamic changes in forest  
 184 area in each climatic zone from 1990 to 2020. For each year, the left solid stacked bar represents  
 185 natural forest (NF), and the right hatched stacked bar represents plantation forest (PF). Bar colors  
 186 indicate the forest area contributed by different climatic zones. The value at the top of each year  
 187 indicates the total national forest area, and labels with “K” denote  $10^3$  km<sup>2</sup>.

## 188 2.3. Methods

### 189 2.3.1. VPD calculation

190 Vapor pressure deficit (VPD, hPa) is expressed, as follows, as the difference between  
 191 saturation vapor pressure ( $P_s$ , hPa) and actual vapor pressure ( $P_w$ , hPa):

$$192 \quad VPD = P_s - P_w \quad (1)$$

193 To calculate VPD, we used directly observed meteorological parameters, including air  
 194 temperature ( $T_a$ , °C), relative humidity ( $RH$ , %), and air pressure ( $P_a$ , hPa).  $P_s$  was calculated using  
 195 the improved Magnus equation (Yuan et al., 2019):

$$196 \quad P_s = 6.112 \times f \times e^{\frac{17.67 \times T_a}{T_a + 243.5}} \quad (2)$$

197 Here,  $f$  is the atmospheric pressure enhancement factor, which corrects for the effect of pressure  
 198 on saturation vapor pressure in moist air (Buck, 1981). This coefficient is calculated using  $P_a$  as  
 199 follows:

$$200 \quad f = 1 + 7 \times 10^{-4} + 3.46 \times 10^{-6} \times P_a \quad (3)$$

201  $P_w$  is then derived from  $P_s$  and  $RH$  as follows :

$$202 \quad P_w = P_s \times RH \times \frac{1}{100\%} \quad (4)$$

### 203 **2.3.2. Sensitivity of TF to LAI**

204 We define the transpiration fraction as

$$205 \quad TF = \frac{T}{E} \quad (5)$$

206 In this study, T and E were first aggregated from daily data to annual growing-season totals  
 207 (April–October), and LAI was represented by the corresponding annual growing-season mean. TF  
 208 was then calculated from these annual growing-season quantities, and all subsequent  $\theta$  analyses  
 209 were therefore conducted at the annual growing-season scale rather than at the daily or monthly  
 210 scale.

211 Note that  $TF \in (0,1)$  is bounded. To explicitly account for the inherent nonlinearity and  
 212 saturation in the TF–LAI relationship, we estimated the sensitivity  $\theta$  as a marginal response under  
 213 a bounded nonlinear framework.

214 Within the full period (1990–2020) and within each 11-year moving window, we fit a quadratic  
 215 model in logit space:

$$216 \quad z = \text{logit}(TF) = \ln\left(\frac{TF}{1-TF}\right) = a + b(LAI - LAI_{med}) + c(LAI - LAI_{med})^2 \quad (6)$$

217 Here,  $LAI_{med}$  is the pixel-specific median LAI within the same period (median-centering was  
 218 used to improve numerical stability). Prior to the logit transform,  $TF$  was clipped to  $[\varepsilon, 1 - \varepsilon]$  ( $\varepsilon =$   
 219 0.005) to avoid numerical singularities.

220 We then recovered  $\widehat{TF} = 1 / (1 + e^{-z})$  and computed the marginal sensitivity as

$$221 \quad \theta = \frac{\partial TF}{\partial LAI} = \widehat{TF} (1 - \widehat{TF}) [b + 2c(LAI - LAI_{med})] \quad (7)$$

222 For ease of interpretation, Eq. (7) can be written as

223  $\theta = \underbrace{\widehat{TF}(1-\widehat{TF})}_{damping} \times \underbrace{[b + 2c(LAI - LAI_{med})]}_{\eta}$ , in which the damping term reflects boundary effects

224 and  $\eta$  represents the structural sensitivity in logit space.

225 To separate the position-dependent saturation effect from changes in the shape of the fitted TF-  
 226 LAI relationship, we evaluated (i)  $\theta_{total}$  at  $LAI = LAI_{med}$ , representing the sensitivity under the  
 227 actual state of each pixel and (ii)  $\theta_{clim}$  at a fixed reference  $LAI_{ref}$  (global median LAI), which  
 228 removes the influence of shifting along the TF-LAI curve. Additionally, the boundary component  
 229 was quantified as

$$230 \quad \theta_{bound} = \theta_{total} - \theta_{clim} \quad (8)$$

231 We calculated  $\theta$  at two time scales. (1) The full-period mean  $\theta$  characterized the average state  
 232 during 1990–2020. (2) The  $\theta$  time series characterized decadal changes, generated using an 11-year  
 233 moving window recorded for the central year (1995–2015), a data processing step that was also used  
 234 for subsequent trend and attribution analyses. Pixels with insufficient valid years and negligible LAI  
 235 variability were excluded to ensure robustness.

236 We further used a fixed-curve counterfactual decomposition to separate the temporal change  
 237 in  $\theta_{total}$  into a position/saturation effect and a shape effect. The position effect describes changes in  
 238  $\theta$  caused by LAI moving along an otherwise fixed TF-LAI curve, and therefore reflects the bounded  
 239 nature of TF and the saturation compression associated with  $TF(1-TF)$ . In contrast, the shape effect  
 240 describes changes in  $\theta$  caused by temporal changes in the fitted TF-LAI curve itself, as reflected by  
 241 changes in the logit-quadratic coefficients.

242 For each forest type, the first 11-year window was used as the reference curve. The fixed-curve  
 243 prediction was calculated by holding the regression coefficients of this reference curve constant  
 244 while allowing LAI to vary through time. The position effect was then defined as the change  
 245 predicted by this fixed-curve model, whereas the shape effect was defined as the residual between  
 246 the observed  $\theta_{total}$  trajectory and the fixed-curve prediction. Thus,

$$247 \quad \Delta\theta_{total} = \Delta\theta_{position} + \Delta\theta_{shape} \quad (9)$$

248 Where  $\Delta\theta_{position}$  represents movement along a fixed bounded response curve and  $\Delta\theta_{shape}$   
 249 represents changes in the response-curve shape.

### 250 **2.3.3. Spatial association under the joint SM–VPD gradient: binning analysis**

251 To assess the relative roles of SM and VPD in the spatial differentiation of  $\theta$ , we applied a  
252 pooled spatial-binning analysis. Using all eligible pure NF and pure PF pixels as samples, we  
253 extracted the full-period mean  $\theta$ , SM, and VPD values and Z-score standardized them. To evaluate  
254 the relative effect of VPD under comparable SM backgrounds, denoted as  $\Delta\theta(\text{VPD}|\text{SM})$ , pixels  
255 were first grouped into bins according to SM. Within each SM bin, the difference in mean  $\theta$  between  
256 high- and low-VPD groups was calculated, and these differences were then averaged across bins.  
257 The relative effect of SM, denoted as  $\Delta\theta(\text{SM}|\text{VPD})$ , was evaluated in the same way by binning  
258 pixels according to VPD and then comparing high- and low-SM groups within each bin. This  
259 approach thus summarized spatial contrasts under comparable hydroclimatic backgrounds using a  
260 control-variable logic. These analyses are complementary but not identical to the subsequent  
261 temporal attribution analyses; specifically, the binning analysis characterized cross-site contrasts in  
262  $\theta$  across the long-term SM–VPD climate space, whereas the partial-correlation and ridge analyses  
263 quantified within-pixel temporal associations of  $\theta$  with SM and VPD.

### 264 **2.3.4. Dynamic temporal attribution: partial correlation and ridge regression**

265 To investigate the pixel-scale temporal relationships of SM and VPD with  $\theta$ , we used partial  
266 correlation and ridge regression based on the 1995–2015 11-year sliding-window series. This  
267 analysis was conducted at two levels. First, for each pixel, we calculated an overall partial  
268 correlation coefficient and ridge-regression coefficient based on the full 1995–2015 series,  
269 representing the average independent association of SM and VPD with  $\theta$  throughout that period  
270 after accounting for their covariation. Second, to evaluate change over time, we performed a  
271 secondary sliding-window analysis on the same 1995–2015 series and generated time series of the  
272 coefficients themselves. Trends in these coefficient series were then used to infer whether the effects  
273 of SM and VPD became stronger or weaker over time. Thus, the first-level analysis described the  
274 mean temporal attribution pattern, whereas the second-level analysis characterized its change over  
275 time.

276 Partial correlation analysis: We calculated two pixel-wise partial correlation coefficients:  $r(\theta,$   
277  $\text{SM}|\text{VPD})$  and  $r(\theta, \text{VPD}|\text{SM})$ . The former represents the correlation between  $\theta$  and SM after  
278 controlling for interannual VPD fluctuations, whereas the latter represents the correlation between

279  $\theta$  and VPD after controlling for SM variability.

280 Ridge regression analysis: Given the collinearity between SM and VPD, we further employed  
281 a ridge regression model,  $\theta = \beta_{SM} \cdot SM + \beta_{VPD} \cdot VPD$ , to more robustly quantify their relative  
282 contributions to  $\theta$ . By introducing an L2 regularization term, ridge regression stabilizes coefficient  
283 estimates under multicollinearity. The regression was performed on standardized time series, and  
284 the resulting coefficients ( $\beta_{SM}$  and  $\beta_{VPD}$ ) directly reflect the relative strengths of the SM and VPD  
285 effects. We further calculated the relative contribution (RC) of SM and VPD as  
286  $RC_{SM} = |\beta_{SM}| / (|\beta_{SM}| + |\beta_{VPD}|)$  and  $RC_{VPD} = |\beta_{VPD}| / (|\beta_{SM}| + |\beta_{VPD}|)$ , to determine the  
287 dominant hydrological driver at each pixel. To further diagnose multicollinearity between SM and  
288 VPD, we also calculated the variance inflation factor (VIF).

289 To quantify temporal changes in  $\theta$  and in the coefficient series derived from the 11-year  
290 moving-window analysis, we estimated trends using the Theil–Sen median slope estimator. Trend  
291 significance was assessed using the Mann–Kendall (MK) test (two-tailed,  $\alpha = 0.05$ ). To reduce  
292 potential bias caused by temporal autocorrelation, the MK statistic was variance-corrected. The  
293 same trend-analysis framework was applied consistently to all moving-window-derived time series  
294 used in the temporal attribution analysis.

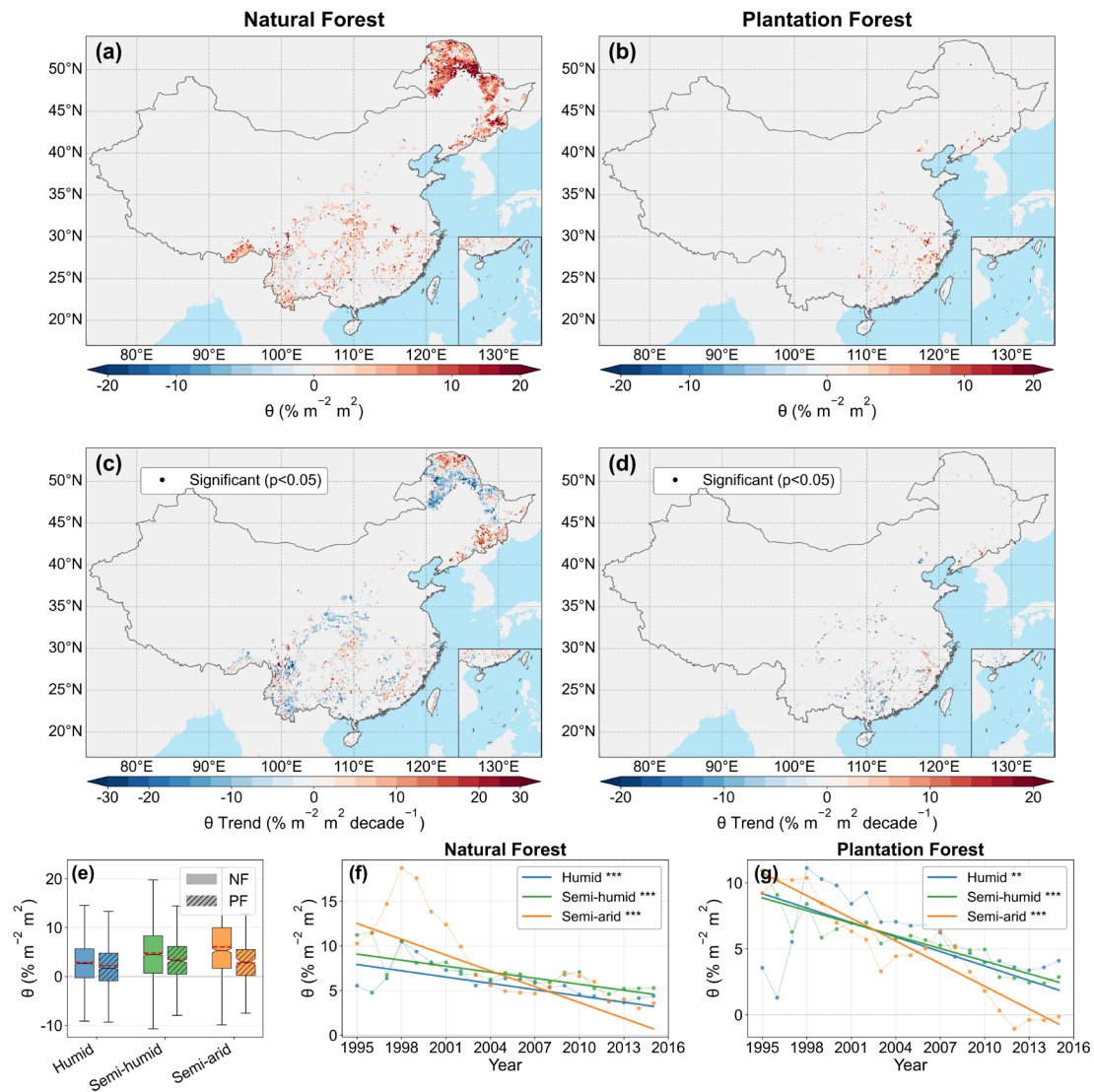
### 295 **2.3.5. Pathway analysis of macroclimate effects on $\theta$**

296 To analyze the pathways through which macroclimate change may affect  $\theta$  via local  
297 hydrological processes, we constructed a pathway model. The independent variable  $X$  served as the  
298 climate-factor trend (including P, Ta, Rn, and WS), the mediator variable  $M$  corresponded to the  
299 local water supply–demand status (SM and VPD trends), and the dependent variable  $Y$  represented  
300 the  $\theta$  trend. RH was not included separately because its effect on atmospheric water demand is  
301 already represented by VPD. Pathway analysis was used to partition the associations between  
302 macroclimate trends and  $\theta$  into direct effects and indirect effects mediated through SM and VPD.  
303 The statistical significance of all pathway effects was tested by bootstrap resampling (1000  
304 iterations). Because SM and VPD may remain correlated under coupled hydroclimatic conditions,  
305 the pathway coefficients were interpreted as complementary association pathways rather than as a  
306 strict causal separation of two fully independent mediators. This interpretation was further evaluated

307 using a supplementary mediator-specification comparison based on SM-only, VPD-only, and joint  
 308 pathway models (Figure S19). The trends of P, Ta, Rn, WS, SM, VPD, and  $\theta$  used in the pathway  
 309 analysis were all estimated using the same Theil–Sen and variance-corrected Mann–Kendall  
 310 framework described above.

### 311 3. Results

#### 312 3.1. Spatiotemporal patterns and long-term trends of $\theta$

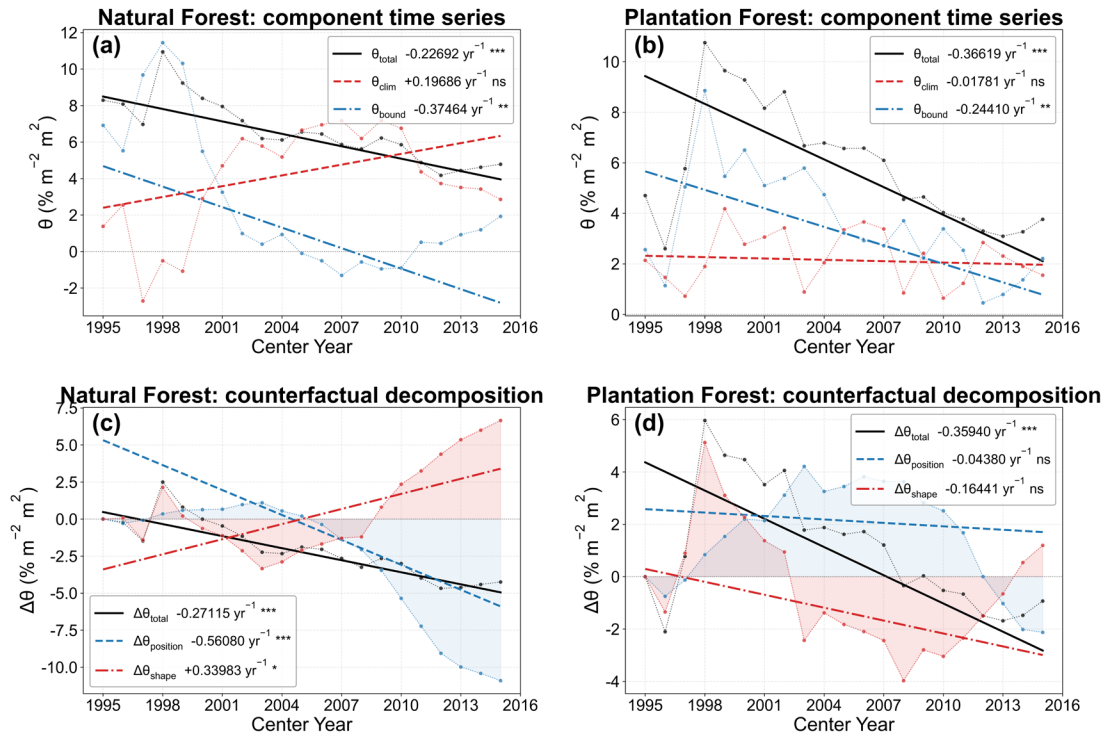


313  
 314 **Figure 3. Spatiotemporal patterns and long-term trends of LAI–TF sensitivity ( $\theta$ ) in China's**  
 315 **natural forests (NF) and plantation forests (PF) during the 1990–2020 growing seasons. (a)**  
 316 **and (b) show the multi-year mean spatial distribution of  $\theta$  for NF and PF, respectively, derived from**  
 317 **the overall logit–quadratic model using  $T_{FE}$ . (c) and (d) show the corresponding long-term trends**  
 318 **in  $\theta$  estimated from the 11-year moving-window time series using the Theil–Sen slope; black dots**

319 indicate significant trends based on the Mann–Kendall test ( $p < 0.05$ ). (e) shows the distribution of  
320  $\theta$  across climatic zones (humid, semi-humid, and semi-arid) for NF and PF. (f) and (g) show the  
321 temporal evolution of zone-averaged  $\theta$  for NF and PF, respectively, with Theil–Sen trend lines  
322 overlaid.

323 Mean  $\theta$  showed clear spatial heterogeneity and was consistently higher in NF than in PF  
324 (Figure 3a, b, e). High- $\theta$  areas in NF were concentrated mainly within the semi-arid to semi-humid  
325 transition belt, whereas PF showed a distinctly more fragmented pattern. During 1990–2020,  
326 growing-season  $\theta$  declined widely in both forest types, with a stronger mean decline in PF than in  
327 NF (Figure 3c, d). Significant negative trends were concentrated mainly in semi-humid and semi-  
328 arid transition regions, while humid regions showed weaker negative trends. The zone-averaged  
329 time series further confirmed that  $\theta$  decreased significantly across climatic zones in both forest types,  
330 with the strongest declines occurring under drier climatic conditions (Figure 3f, g). Overall, the  
331 marginal enhancement of TF by increasing LAI weakened over the past three decades, especially in  
332 PF and in relatively dry regions.

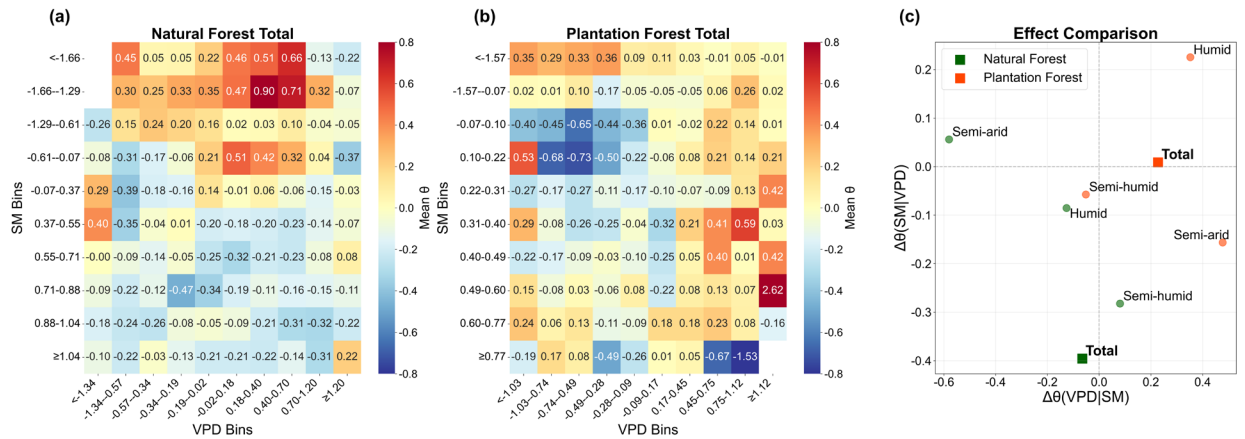
333 The decomposition of  $\theta_{\text{total}}$  provided additional insight into the mechanisms behind the  
334 observed decline (Figure 4). Under the main TFE definition, the long-term decrease in  $\theta_{\text{total}}$  reflected  
335 both position-dependent saturation and changes in the fitted TF–LAI curve shape, but their relative  
336 roles differed between forest types. In natural forests, the position/saturation component made a  
337 negative contribution to  $\theta_{\text{total}}$ , whereas the shape component differed in sign and partly offset the  
338 decline. This contrast indicates that the total  $\theta$  trend would be difficult to interpret from  $\theta_{\text{total}}$  alone.  
339 In plantation forests, the position/saturation component also contributed to the weakening of  $\theta_{\text{total}}$ ,  
340 while the shape component indicated additional changes in the fitted TF–LAI sensitivity. These  
341 results show that the weakening of the LAI enhancement effect on TF is not merely a bounded  
342 geometric consequence of higher LAI or TF approaching saturation; it also reflects changes in the  
343 biophysical TF–LAI relationship under evolving hydroclimatic conditions.



344

345 **Figure 4. Decomposition of temporal changes in LAI–TF sensitivity ( $\theta$ ) into**  
 346 **position/saturation and shape/climate-related components. (a, b) Time series of spatially**  
 347 **averaged  $\theta_{\text{total}}$ ,  $\theta_{\text{clim}}$ , and  $\theta_{\text{bound}}$  for natural forests (NF) and plantation forests (PF), respectively,**  
 348 **under the main TFE definition. (c, d) Counterfactual decomposition of  $\Delta\theta_{\text{total}}$  into  $\Delta\theta_{\text{position}}$  and**  
 349  **$\Delta\theta_{\text{shape}}$  for NF and PF, respectively. The fixed-curve null model holds the logit-quadratic regression**  
 350 **coefficients at their first-window values while allowing LAI to vary, so  $\Delta\theta_{\text{position}}$  reflects movement**  
 351 **along a fixed bounded TF–LAI curve.  $\Delta\theta_{\text{shape}}$  is the residual between the observed trajectory and the**  
 352 **fixed-curve prediction and reflects changes in the fitted response-curve shape. Lines indicate Theil–**  
 353 **Sen trends; significance was evaluated using the Mann–Kendall test.**

354 **3.2. Hydroclimatic controls of  $\theta$ : SM and VPD**  
 355 **3.2.1. Response of  $\theta$  to the joint SM–VPD gradient**



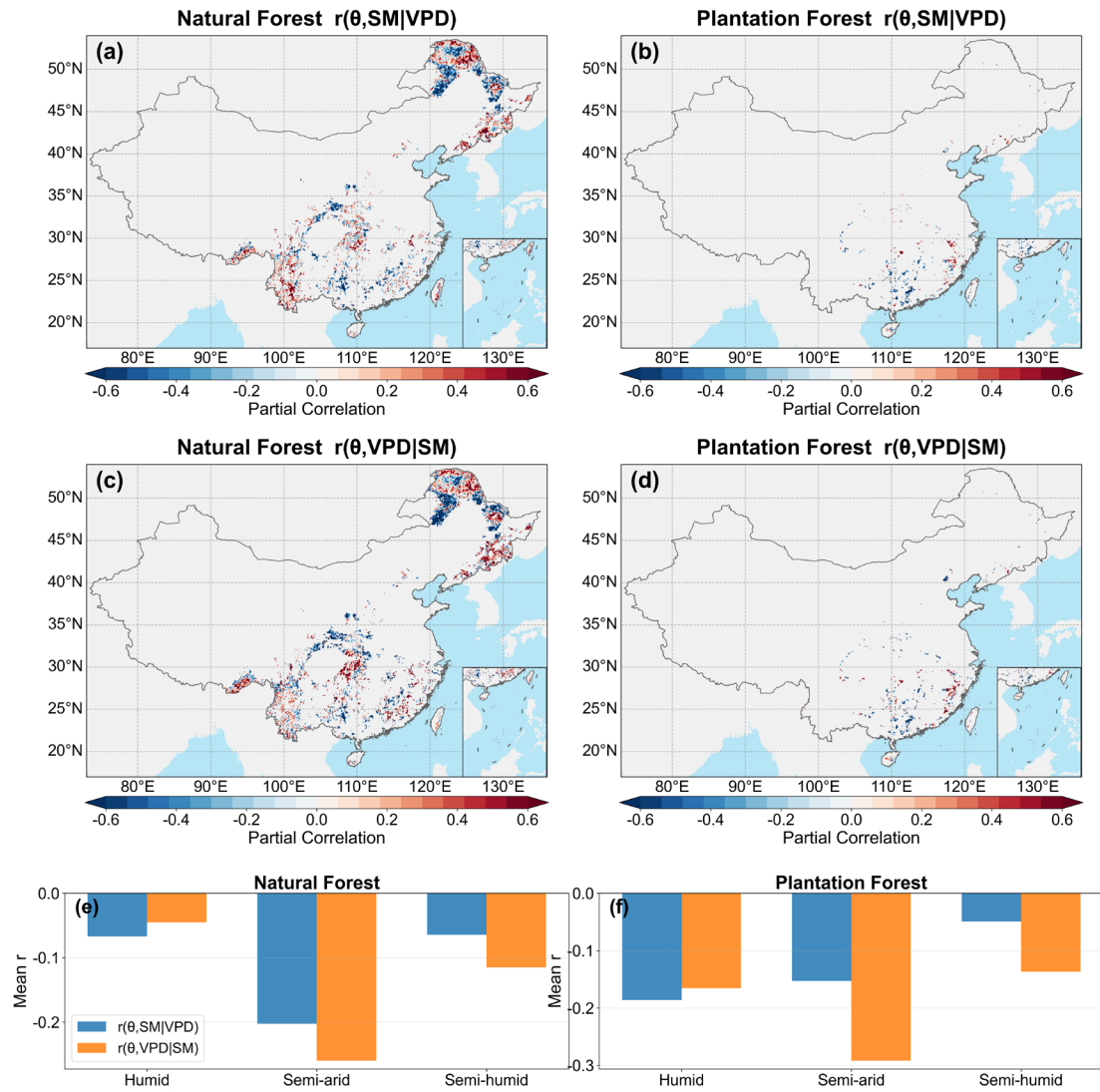
356  
 357 **Figure 5. Pooled spatial binning analysis of LAI–TF sensitivity ( $\theta$ ) under the joint soil**  
 358 **moisture (SM)–vapor pressure deficit (VPD) gradient during the 1990–2020 growing seasons.**  
 359 (a) and (b) show the mean standardized  $\theta$  values in  $10 \times 10$  SM–VPD bins for natural forests (NF)  
 360 and plantation forests (PF), respectively; only bins with sample size  $\geq 10$  are shown. (c) shows the  
 361 relative effects of VPD and SM as indicated by  $\Delta\theta(\text{VPD}|\text{SM})$  and  $\Delta\theta(\text{SM}|\text{VPD})$ , calculated from  
 362 the top 20% versus bottom 20% contrasts within each bin and then averaged across bins. Circles  
 363 denote climatic zones, while squares denote the national total.  $\theta$  was Z-score standardized in this  
 364 analysis.

365 Pooled binning analysis showed that  $\theta$  varied nonlinearly along the joint SM–VPD gradient in  
 366 both forest types, with relatively high values occurring under intermediate SM and moderate-to-  
 367 high VPD conditions, and lower values toward both the wet/low-VPD and dry/high-VPD ends of  
 368 the gradient (Figure 5a,b). The contrast analysis further revealed clear differences in the relative  
 369 effects of SM and VPD (Figure 5c). At the national scale, NF showed a much stronger SM-related  
 370 contrast than VPD-related contrast [ $\Delta\theta(\text{SM}|\text{VPD}) = -0.396$  versus  $\Delta\theta(\text{VPD}|\text{SM}) = -0.065$ ], whereas  
 371 PF showed the opposite pattern, with a much stronger VPD-related contrast [ $\Delta\theta(\text{VPD}|\text{SM}) = 0.228$   
 372 versus  $\Delta\theta(\text{SM}|\text{VPD}) = 0.009$ ]. Across climatic zones, NF exhibited stronger VPD-related contrasts  
 373 in the humid and semi-arid zones but stronger SM-related contrasts in the semi-humid zone. In  
 374 contrast, PF was mainly VPD-dominated in the humid and semi-arid zones, while both contrasts  
 375 were relatively weak in the semi-humid zone. Within the pooled spatial-binning framework, these  
 376 results indicate that the relative roles of soil water supply and atmospheric demand differed

377 markedly between NF and PF. Zone-specific pooled SM–VPD binning patterns for NF and PF are  
378 shown in Figures S14 and S15, respectively.

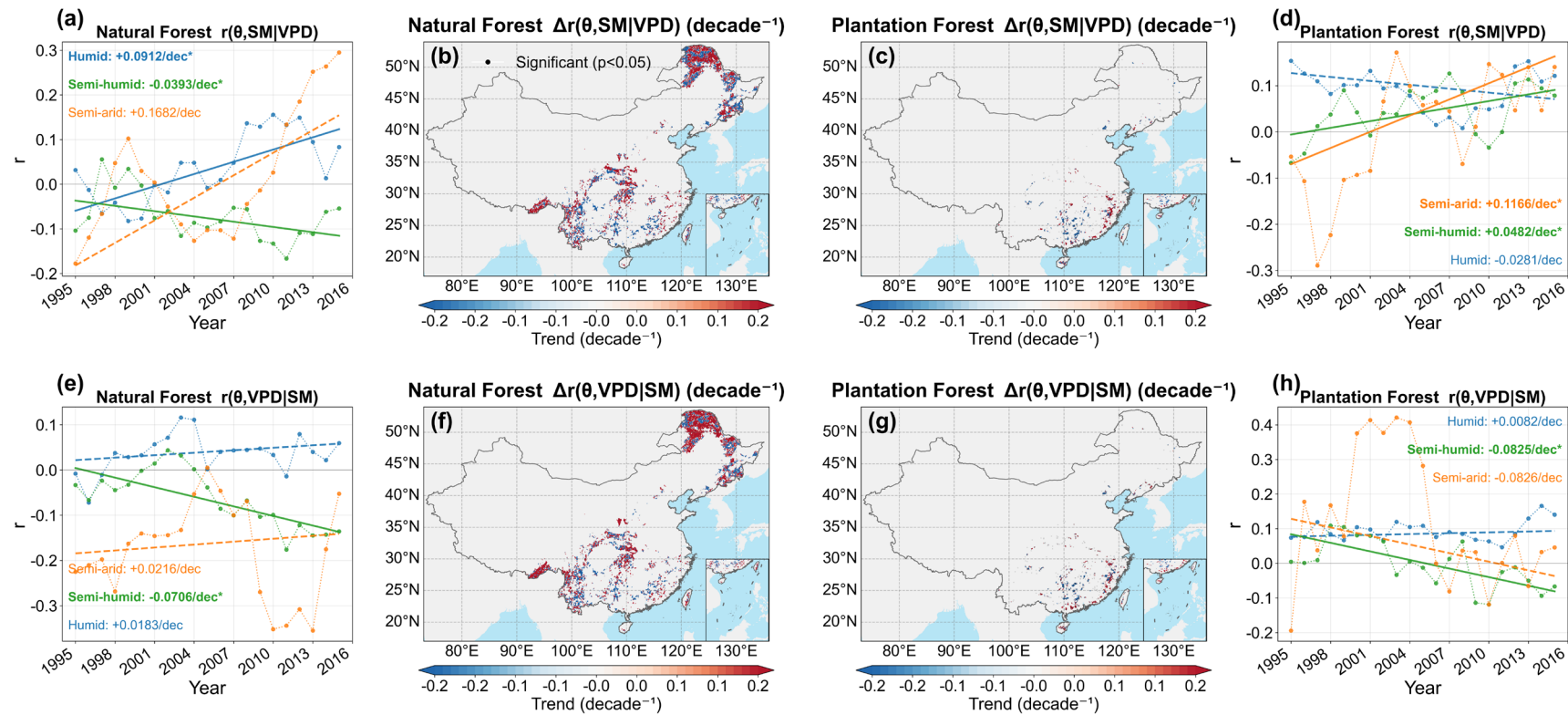
### 379 **3.2.2. Dynamic evolution of the independent effects of SM and VPD**

380 Partial-correlation analysis revealed that the independent associations of  $\theta$  with both SM and  
381 VPD were predominantly negative and were generally stronger in PF than in NF (Figure 6). At the  
382 national scale, the mean values of  $r(\theta, \text{SM}|\text{VPD})$  and  $r(\theta, \text{VPD}|\text{SM})$  were  $-0.0725$  and  $-0.0992$  in  
383 NF, compared with  $-0.1517$  and  $-0.1630$  in PF, respectively, indicating slightly stronger VPD-  
384 related associations in both forest types and overall stronger hydroclimatic constraints in PF. Across  
385 climatic zones, the strongest negative partial correlations in NF occurred in the semi-arid zone,  
386 especially for VPD, whereas PF showed consistently negative correlations across all zones. The  
387 temporal analyses further revealed spatially heterogeneous changes in these relationships (Figure  
388 7). In NF, the SM-related partial correlation became less negative in the humid and semi-arid zones,  
389 while the VPD-related partial correlation also became less negative in the semi-humid zone. In PF,  
390 the SM-related partial correlation became more negative in the semi-humid and semi-arid zones,  
391 whereas the VPD-related partial correlation became less negative in the semi-humid zone. Overall,  
392 both SM and VPD constrained  $\theta$ , but the constraints were generally stronger in PF, and their  
393 temporal changes were regionally differentiated rather than spatially uniform.



394

395 **Figure 6. Spatial distribution and zonal means of partial correlations between forest LAI-TF**  
 396 **sensitivity ( $\theta$ ) and hydroclimatic factors during the growing season from 1995 to 2015. (a) and**  
 397 **(b) show the spatial patterns of  $r(\theta, SM|VPD)$  for natural forests (NF) and plantation forests (PF),**  
 398 **respectively; (c) and (d) show the corresponding patterns of  $r(\theta, VPD|SM)$ . (e) and (f) show the**  
 399 **mean partial correlations across climatic zones. All variables were Z-score standardized before**  
 400 **analysis, and pixels with fewer than 10 years of valid data were excluded.**



401

402

**Figure 7. Temporal evolution and spatial trends of partial correlations between forest LAI–TF sensitivity ( $\theta$ ) and hydroclimatic factors during the growing**

403

**season from 1995 to 2015. (a) and (d) show the temporal evolution of zone-averaged  $r(\theta, SM|VPD)$  for NF and PF, respectively; (b) and (c) show the corresponding**

404

**spatial trends. (e) and (h) show the temporal evolution of zone-averaged  $r(\theta, VPD|SM)$  for NF and PF, respectively; (f) and (g) show the corresponding spatial trends.**

405

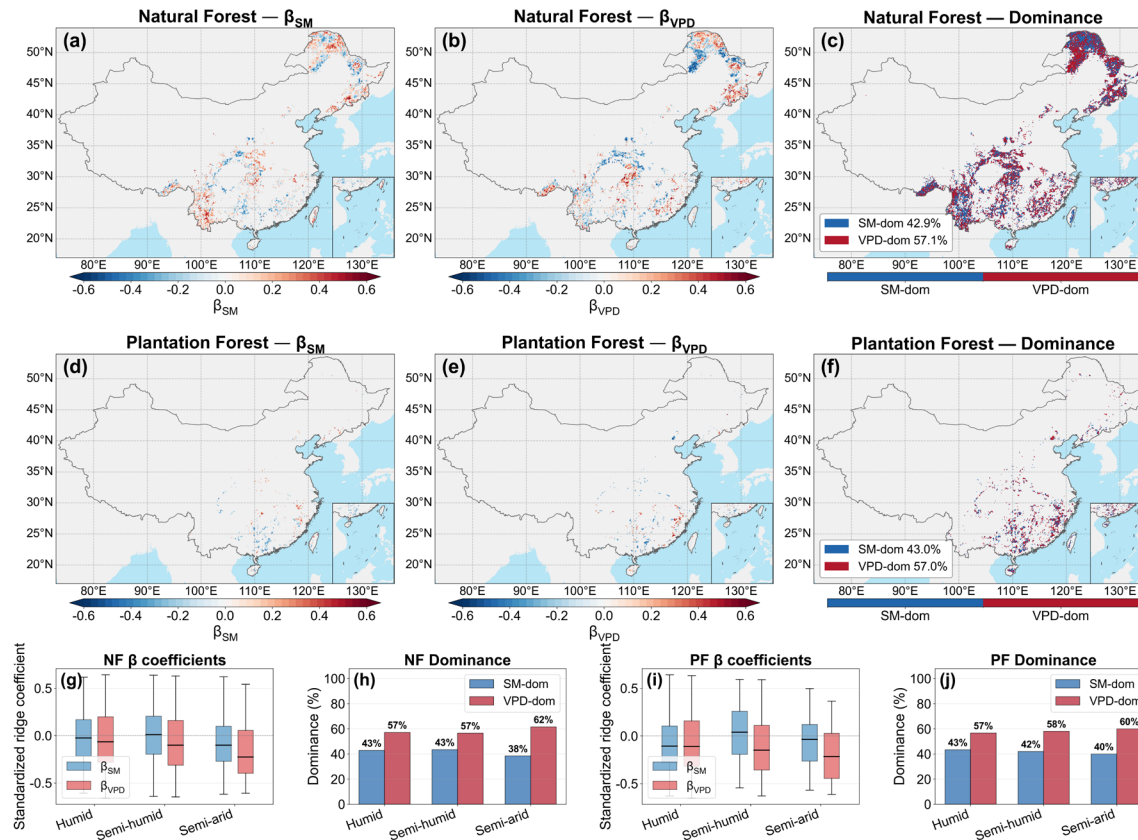
**Trend slopes were estimated using the Theil–Sen estimator, and significant pixels according to the variance-corrected Mann–Kendall test ( $p < 0.05$ ) are indicated by**

406

**black dots.**

407 **3.2.3. Quantification and spatiotemporal heterogeneity of dominant**  
408 **hydrological drivers**

409 Ridge regression showed that both SM and VPD were generally negatively associated with  $\theta$ ,  
410 but the magnitude was usually stronger for VPD (Figure 8). At the national scale, both NF and PF  
411 remained slightly more VPD-dominated in terms of the present spatial pattern, with mean relative  
412 contributions of VPD of 0.541 and 0.534 in NF and PF, respectively. Consistently, VPD-dominated  
413 pixels accounted for 57.1% of all NF pixels and 57.0% of all PF pixels, compared with 42.9% and  
414 43.0%, respectively, for SM-dominated pixels. The relative-contribution and dominance statistics  
415 therefore consistently indicated a modest present-day advantage of VPD over SM, particularly in  
416 the semi-arid zone. The trend analysis further indicated a general strengthening of the SM effect  
417 and a weakening of the VPD effect in several regions, especially across semi-humid to semi-arid  
418 areas (Figure 9). Within the pixel-wise temporal analysis, these results suggest that VPD explained  
419 a slightly larger share of the spatial pattern of  $\theta$ , whereas the relative role of SM increased over time.  
420 RC and VIF supported the robustness of this interpretation (Figure S16).



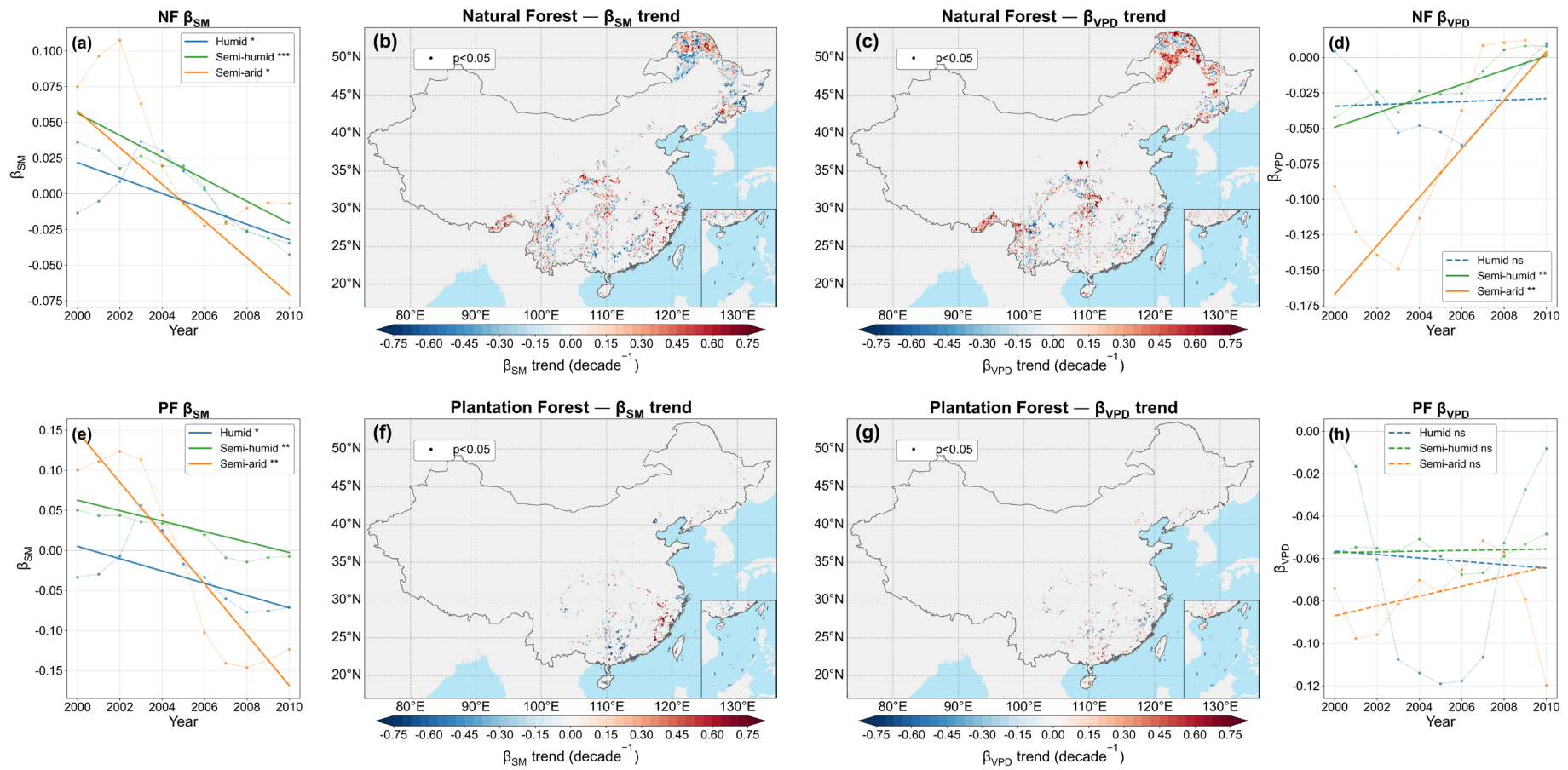
421

422 **Figure 8. Spatial distribution of ridge-regression standardized coefficients and dominant hydrological driver for forest  $\theta$ .** For natural forests (NF), (a) and (b)

423 show the spatial distributions of  $\beta_{SM}$  and  $\beta_{VPD}$ , respectively, and (c) shows the corresponding dominance pattern. (d)–(f) show the same results for plantation forests

424 (PF). (g) and (i) show boxplots of pixel-level standardized  $\beta_{SM}$  and  $\beta_{VPD}$  across climatic zones for NF and PF, respectively. The central line denotes the median, boxes

425 indicate the interquartile range, whiskers extend to 1.5 times the interquartile range, and points outside the whiskers are shown as outliers. (h) and (j) show the fractions  
 426 of SM- and VPD-dominated pixels across climatic zones. Warm colors indicate positive coefficients and cool colors indicate negative coefficients; blue and red in  
 427 dominance maps denote SM-dominated and VPD-dominated pixels, respectively.

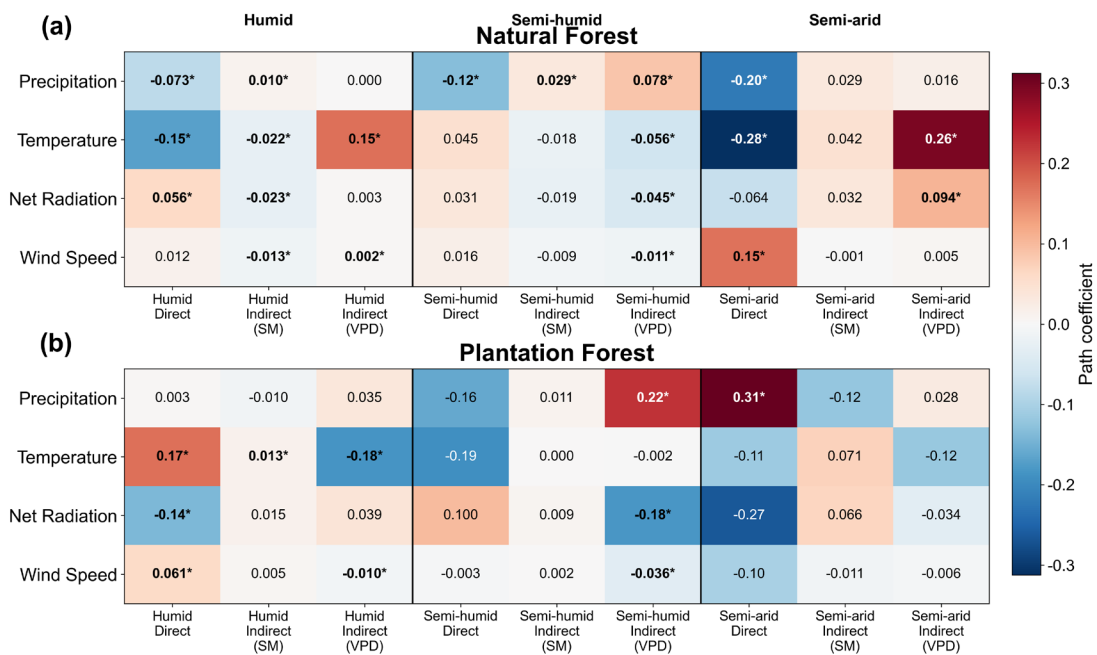


428

429 **Figure 9. Temporal evolution and spatial trends of ridge-regression coefficients for forest  $\theta$ .** (a) and (e) show the temporal evolution of zone-averaged  $\beta_{SM}$  for NF  
430 and PF, respectively; (b) and (f) show the corresponding spatial trends in  $\beta_{SM}$ . (d) and (h) show the temporal evolution of zone-averaged  $\beta_{VPD}$  for NF and PF, respectively;  
431 (c) and (g) show the corresponding spatial trends in  $\beta_{VPD}$ . Trend slopes were estimated using the Theil–Sen estimator, and significant pixels based on the Mann–Kendall  
432 test ( $p < 0.05$ ) are indicated by black dots. Solid trend lines indicate significant trends, and dashed lines indicate non-significant trends.

433 **3.3. Pathway attribution of macro-climate effects on  $\theta$**

434 Pathway analysis indicated that the effects of macroclimate change on  $\theta$  varied strongly among  
 435 drivers, climatic zones, and forest types (Figure 10). In natural forests (NF), precipitation generally  
 436 showed negative direct effects, especially in the semi-humid and semi-arid zones, while its indirect  
 437 effects differed among pathways, including positive VPD-mediated effects in humid and semi-arid  
 438 zones. Temperature was the most consistent negative direct driver in NF, with particularly strong  
 439 negative effects in humid and semi-arid regions, while its indirect effects differed according to  
 440 pathway, including positive VPD-mediated effects in humid and semi-arid zones. In plantation  
 441 forests (PF), the pathway structure was more heterogeneous; specifically, precipitation showed a  
 442 significant positive direct effect in the semi-arid zone, temperature showed opposite indirect effects  
 443 through SM and VPD in the humid zone, and net radiation and wind speed mainly exerted pathway-  
 444 specific effects in humid and semi-humid regions. Overall, the pathway coefficients indicated strong  
 445 dependence on hydroclimatic context and forest type in how macroclimate trends were associated  
 446 with changes in  $\theta$ , with no single pathway dominating across all climate drivers and zones. A  
 447 supplementary mediator-specification comparison showed that the direction of VPD-mediated  
 448 indirect effects was generally more robust across single-mediator and joint models than that of SM-  
 449 mediated effects, whereas SM-mediated pathways were more sensitive to model specification under  
 450 SM–VPD coupling (Figure S19).



451

452 **Figure 10. Heatmap of pathway coefficients across climate zones for natural and plantation**  
453 **forests.** Standardized path coefficients show the decomposition of the effects of four macroclimate  
454 drivers (precipitation, temperature, net radiation, and wind speed) on  $\theta_{\text{total}}$  trends into direct effects  
455 and indirect effects mediated by SM and VPD for natural forests (a) and plantation forests (b). Rows  
456 correspond to the four macro-climate drivers, while columns are grouped by climate zone (humid,  
457 semi-humid, and semi-arid), each subdivided into direct effects, indirect effects via SM, and indirect  
458 effects via VPD. Cell values are standardized coefficients from parallel dual-mediation pathway  
459 analysis, and asterisks indicate significance at the 95% level (i.e., bootstrap confidence interval  
460 excludes zero). Warm colors indicate positive effects, while cool colors indicate negative effects.

## 461 **4. Discussion**

### 462 **4.1. Nonlinear hydroclimatic regulation of $\theta$**

463 The joint SM–VPD analysis shows that  $\theta$  was highest under intermediate SM and moderate-  
464 to-high VPD, corresponding to relatively strong atmospheric demand, and declined toward both  
465 wetter/low-demand and drier/high-demand conditions (Figure 5; Figures S14–S15). This pattern  
466 indicates that increased leaf area enhances TF most effectively when water supply is sufficient but  
467 not excessive and evaporative demand is strong enough to sustain canopy transpiration. Once soil  
468 water becomes limiting or atmospheric demand becomes too strong, stomatal regulation  
469 increasingly constrains transpiration to avoid hydraulic damage, so the marginal gain in  
470 transpiration per unit increase in LAI declines (Novick et al., 2016; Grossiord et al., 2020;  
471 McDowell et al., 2022). Under wetter and weak-demand conditions, the capacity of additional leaf  
472 area to increase TF is also reduced because energy limitations, weaker canopy–atmosphere coupling,  
473 and larger non-transpirational evaporation fractions all weaken the translation of additional leaf area  
474 into transpiration (Konings et al., 2017; Stoy et al., 2019). The  $\theta$  decomposition and supplementary  
475 diagnostics further suggest that this nonlinearity cannot be explained solely as a bounded geometric  
476 effect of TF; part of the long-term change also reflects shifts in the LAI–TF relationship itself  
477 (Figure 4; Figures S6–S13).

### 478 **4.2. Long-term weakening of the LAI enhancement effect on TF**

479 The widespread decline in  $\theta$ , especially across semi-humid to semi-arid transition zones,  
480 indicates that the capacity of increasing LAI to enhance TF has weakened over the last three decades

481 (Figure 3). This trend is consistent with a background of warming, rising VPD, and increasing  
482 frequency of soil moisture limitation, all of which reduce the effective transpiration response of  
483 forests to additional canopy development (Yuan et al., 2019; Lian et al., 2020; Denissen et al., 2022).  
484 Rising atmospheric CO<sub>2</sub> may also have contributed to this decline by lowering stomatal conductance  
485 and increasing intrinsic water-use efficiency, thereby reducing transpiration demand per unit leaf  
486 area even where greening continued (Keenan et al., 2013; Keenan et al., 2016; Lavergne et al., 2019;  
487 Liang et al., 2023). At the same time, the supplementary analyses are more consistent with  
488 interpreting CO<sub>2</sub> as a temporally coherent background forcing rather than a spatially heterogeneous  
489 driver of  $\theta$  across China's forests (Figure S17; Table S1). Stand development may likewise have  
490 modulated this trajectory. Age-related changes in stand structure, rooting depth, canopy roughness,  
491 and interception can shift the partitioning of evapotranspiration between transpiration and non-  
492 transpirational components, and therefore alter the LAI–TF relationship even without large changes  
493 in total leaf area (Fan et al., 2017; Forrester, 2015). However, the age-stratified results show that the  
494 higher  $\theta$  in NF than in PF persisted across age groups, and including stand age did not overturn the  
495 broad interpretation of the relative roles of SM and VPD, although the magnitude of change was  
496 heterogeneous across forest types and climatic zones (Figure S18; Table S2). Together, these results  
497 suggest that CO<sub>2</sub> rise and stand development may act as background modifiers of  $\theta$ , while the  
498 dominant large-scale patterns remain primarily associated with hydroclimatic variability.

### 499 **4.3. Temporal changes in hydroclimatic effects on $\theta$**

500 Partial correlation, ridge regression, and pathway analysis consistently indicate that the  
501 hydroclimatic controls on  $\theta$  have changed over time, with the relative role of SM strengthening and  
502 that of VPD weakening in many regions (Figures 6–10). This does not mean that atmospheric  
503 demand has ceased to matter; VPD still explains a slightly larger share of the present spatial pattern  
504 of  $\theta$ , as also supported by the dominance statistics and multicollinearity diagnostics (Figure 8;  
505 Figure S16). The more important point is that the sensitivity of  $\theta$  to soil moisture limitation has  
506 intensified under recent climatic conditions. This interpretation is physically consistent with the  
507 increasing prevalence of water-limited ecosystem behavior under warming, in which rising  
508 evaporative demand is increasingly translated into ecological stress through soil-water depletion  
509 rather than through atmospheric forcing alone (Berg et al., 2016; Denissen et al., 2022). Once

510 ecosystems approach critical soil-moisture thresholds more frequently, stomatal and hydraulic  
511 regulation become more tightly constrained by water supply, and the explanatory role of SM rises  
512 accordingly (Fu et al., 2022; Liu et al., 2025). The pathway results add the same message at a broader  
513 scale: temperature exerted generally negative effects on  $\theta$ , whereas the effects of precipitation and  
514 radiation varied by forest type and climatic zone, implying that macroclimate trends influence  $\theta$   
515 through multiple hydroclimatic pathways rather than through a single dominant mechanism.

#### 516 **4.4. Contrasting ecohydrological responses of natural and plantation forests**

517 The contrast between natural and plantation forests remained one of the clearest features of the  
518 analysis. NF consistently showed higher  $\theta$ , and high- $\theta$  values in NF were maintained across a wider  
519 range of SM–VPD backgrounds, whereas PF showed lower  $\theta$  and a more restricted range of  
520 hydroclimatic conditions under which high  $\theta$  occurred. This pattern likely reflects differences  
521 between long-term spatial hydroclimatic contrasts and within-pixel temporal variability. Spatial  
522 contrasts integrate longer-term differences in stand structure, species composition, hydraulic  
523 diversity, and belowground water access, whereas temporal anomalies are expressed more directly  
524 through canopy–atmosphere coupling and stomatal–hydraulic regulation during drought (Martínez-  
525 Vilalta & García-Forner, 2017; Grossiord et al., 2020; Novick et al., 2024; Bachofen et al., 2024).  
526 Under this interpretation, the broader hydroclimatic response of NF may reflect the greater structural  
527 and functional heterogeneity often associated with natural forests, while the narrower response of  
528 PF may reflect the relative structural simplification typical of many plantation stands. This  
529 interpretation is also consistent with evidence that higher hydraulic diversity can buffer ecosystem  
530 drought responses (Anderegg et al., 2018). The age-stratified supplementary results are consistent  
531 with this interpretation, because the higher  $\theta$  in NF than in PF persisted across age classes and this  
532 pattern is therefore unlikely to be explained solely by stand age.

#### 533 **4.5. Implications and limitations**

534 These results imply that further greening will not necessarily translate into proportionally  
535 higher transpiration fractions under continued warming and drying. In regions where hydroclimatic  
536 water stress is increasing, especially across semi-humid to semi-arid transition zones, the  
537 ecohydrological consequences of increasing canopy leaf area depend increasingly on soil water

538 supply, and this dependence appears more evident in plantation forests than in natural forests. This  
539 has direct management implications: plantation design may benefit from greater rooting-depth and  
540 trait diversity and from stand structures that reduce rapid soil-water depletion, whereas natural  
541 forests may benefit more from maintaining multilayer canopy structure and hydraulic diversity  
542 under rising atmospheric demand. Several limitations should remain explicit. A nationwide in situ  
543 benchmark for  $\theta$  trends is not yet available because long-term observations that simultaneously  
544 resolve transpiration partitioning, LAI dynamics, and stand development remain too sparse across  
545 China's forests. We therefore evaluated robustness through cross-product consistency rather than  
546 direct site-based validation. In addition, because  $\theta$ , SM, and VPD were analyzed from growing-  
547 season aggregates and moving-window series, the results characterize seasonal-to-interannual  
548 hydroclimatic controls rather than instantaneous stomatal responses to short-lived atmospheric  
549 fluctuations. Even with these constraints, the convergence among the main analyses, the  
550 supplementary robustness checks, and the CO<sub>2</sub>- and age-sensitivity diagnostics supports the central  
551 inference that the enhancement of TF by increasing LAI has weakened across China's forests and  
552 is increasingly shaped by soil moisture limitation.

## 553 **5. Conclusion**

554 Across China's forests, the enhancement of TF caused by increased LAI has weakened during  
555 1990–2020. VPD still explains a slightly larger share of the present spatial pattern of  $\theta$ , but the role  
556 of SM has strengthened over this timespan, indicating there has been an increase in SM limitation.  
557 Differences between NF and PF were obvious: NF maintained higher  $\theta$  values, whereas PF showed  
558 a greater long-term decline in  $\theta$ . Collectively, these results indicate that continued greening under  
559 warming will not necessarily result in proportionally higher TF, particularly in semi-humid to semi-  
560 arid transition regions.

## 561 **Author contributions**

562 Xiao Zhang performed the analysis, prepared the figures, and drafted the manuscript. Xinxiao  
563 Yu contributed to the study design, interpretation of the results, and manuscript revision. Guodong  
564 Jia conceived and supervised the study, contributed to the analytical framework, and revised the  
565 manuscript. All authors discussed the results and approved the final manuscript.

566 **Competing interests**

567 The authors declare that they have no conflict of interest.

568 **Code and data availability**

569 The datasets used in this study are publicly available from the sources cited in Table 1. The  
570 processed data and code supporting the findings of this study are available from the corresponding  
571 author upon reasonable request.

572 **Funding**

573 This research was supported by the National Natural Science Foundation of China (grant  
574 numbers 42277062, 41977149, and 42230714).

575

576 **References**

- 577       Anderegg, W.R.L., Konings, A.G., Trugman, A.T., Yu, K., Bowling, D.R., Gabbitas, R., Karp,  
578 D.S., Pacala, S., Sperry, J.S., Sulman, B.N. and Zenes, N. (2018) Hydraulic diversity of forests  
579 regulates ecosystem resilience during drought. *Nature*, 561, 538–541. doi:10.1038/s41586-018-  
580 0539-7
- 581       Bachofen, C., Tumber-Dávila, S.J., Mackay, D.S., McDowell, N.G., Carminati, A., Klein, T.,  
582 Stocker, B.D., Mencuccini, M. and Grossiord, C. (2024) Tree water uptake patterns across the globe.  
583 *New Phytologist*, 242, 1891–1910. doi:10.1111/nph.19762
- 584       Berg, A., Findell, K., Lintner, B., Giannini, A., Seneviratne, S.I., van den Hurk, B., Lorenz, R.,  
585 Pitman, A.J., Hagemann, S., Meier, A., Cheruy, F., Ducharne, A., Malyshev, S. and Milly, P.C.D.  
586 (2016) Land–atmosphere feedbacks amplify aridity increase over land under global warming.  
587 *Nature Climate Change*, 6, 869–874. doi:10.1038/nclimate3029
- 588       Buck, A.L. (1981) New equations for computing vapor pressure and enhancement factor.  
589 *Journal of Applied Meteorology*, 20, 1527–1532. doi:10.1175/1520-  
590 0450(1981)020<1527:NEFCVP>2.0.CO;2
- 591       Cao, S., Li, M., Zhu, Z., Wang, Z., Zha, J., Zhao, W., Duanmu, Z., Chen, J., Zheng, Y., Chen,  
592 Y., Myneni, R.B. and Piao, S. (2023) Spatiotemporally consistent global dataset of the GIMMS leaf  
593 area index (GIMMS LAI4g) from 1982 to 2020. *Earth System Science Data*, 15, 4877–4899.  
594 doi:10.5194/essd-15-4877-2023
- 595       Chen, H., Wei, Y. and Huang, J.J. (2024) Widespread increase in plant transpiration driven by  
596 global greening. *Global and Planetary Change*, 235, 104395. doi:10.1016/j.gloplacha.2024.104395
- 597       Cheng, K., Chen, Y., Xiang, T., Yang, H., Liu, W., Ren, Y., Guan, H., Hu, T., Ma, Q. and Guo,  
598 Q. (2024a) A 2020 forest age map for China with 30 m resolution. *Earth System Science Data*, 16,  
599 803–819. doi:10.5194/essd-16-803-2024
- 600       Cheng, K., Yang, H., Guan, H., Ren, Y., Chen, Y., Chen, M., Yang, Z., Lin, D., Liu, W., Xu,  
601 J., Xu, G., Ma, K. and Guo, Q. (2024b) Unveiling China’s natural and planted forest spatial–  
602 temporal dynamics from 1990 to 2020. *ISPRS Journal of Photogrammetry and Remote Sensing*,  
603 209, 37–50. doi:10.1016/j.isprsjprs.2024.01.024
- 604       Cheng, K., Zhang, Y., Yang, H., Ren, Y., Xiang, T., Chen, Y., Yang, Z., Chen, M., Xu, J.,  
605 Huang, G., Xu, G., Tao, S., Yu, Z. and Guo, Q. (2025) China’s naturally regenerated forests  
606 currently have greater aboveground carbon accumulation rates than newly planted forests.  
607 *Communications Earth & Environment*, 6, 345. doi:10.1038/s43247-025-02323-z
- 608       Denissen, J.M.C., Teuling, A.J., Pitman, A.J., Koirala, S., Migliavacca, M., Li, W., Reichstein,  
609 M., Winkler, A.J., Zhan, C. and Orth, R. (2022) Widespread shift from ecosystem energy to water  
610 limitation with climate change. *Nature Climate Change*, 12, 677–684. doi:10.1038/s41558-022-  
611 01403-8
- 612       Fan, Y., Miguez-Macho, G., Jobbágy, E.G., Jackson, R.B. and Otero-Casal, C. (2017)  
613 Hydrologic regulation of plant rooting depth. *Proceedings of the National Academy of Sciences of*  
614 *the United States of America*, 114, 10572–10577. doi:10.1073/pnas.1712381114
- 615       Farooq, T.H., Shakoor, A., Wu, X., Li, Y., Rashid, M.H.U., Zhang, X., Gilani, M.M., Kumar,  
616 U., Chen, X. and Yan, W. (2021) Perspectives of plantation forests in the sustainable forest

617 development of China. *iForest - Biogeosciences and Forestry*, 14, 166–174. doi:10.3832/ifor3551-  
618 014

619 Forrester, D.I. (2015) Transpiration and water-use efficiency in mixed-species forests versus  
620 monocultures: effects of tree size, stand density and season. *Tree Physiology*, 35, 289–304.  
621 doi:10.1093/treephys/tpv011

622 Fu, Z., Ciais, P., Feldman, A., Gentine, P., Makowski, D., Prentice, I.C., Stoy, P.C., Bastos, A.  
623 and Wigneron, J.-P. (2022) Critical soil moisture thresholds of plant water stress in terrestrial  
624 ecosystems. *Science Advances*, 8, eabq7827. doi:10.1126/sciadv.abq7827

625 Grossiord, C., Buckley, T.N., Cernusak, L.A., Novick, K.A., Poulter, B., Siegwolf, R.T.W.,  
626 Sperry, J.S. and McDowell, N.G. (2020) Plant responses to rising vapor pressure deficit. *New  
627 Phytologist*, 226, 1550–1566. doi:10.1111/nph.16485

628 Hu, Y., Wei, F., Fu, B. and Zhang, W. (2023) Ecosystems in China have become more sensitive  
629 to changes in water demand since 2001. *Communications Earth & Environment*, 4, 444.  
630 doi:10.1038/s43247-023-01105-9

631 Keenan, T.F., Hollinger, D.Y., Bohrer, G., Dragoni, D., Munger, J.W., Schmid, H.P. and  
632 Richardson, A.D. (2013) Increase in forest water-use efficiency as atmospheric carbon dioxide  
633 concentrations rise. *Nature*, 499, 324–327. doi:10.1038/nature12291

634 Keenan, T.F., Prentice, I.C., Canadell, J.G., Williams, C.A., Wang, H., Raupach, M. and  
635 Collatz, G.J. (2016) Recent pause in the growth rate of atmospheric CO<sub>2</sub> due to enhanced terrestrial  
636 carbon uptake. *Nature Communications*, 7, 13428. doi:10.1038/ncomms13428

637 Koehler, T., Wankmüller, F.J.P., Sadok, W. and Carminati, A. (2023) Transpiration response  
638 to soil drying versus increasing vapor pressure deficit in crops: physical and physiological  
639 mechanisms and key plant traits. *Journal of Experimental Botany*, 74, 4789–4807.  
640 doi:10.1093/jxb/erad221

641 Konings, A.G., Williams, A.P. and Gentine, P. (2017) Sensitivity of grassland productivity to  
642 aridity controlled by stomatal and xylem regulation. *Nature Geoscience*, 10, 284–288.  
643 doi:10.1038/ngeo2903

644 Lavergne, A., Graven, H., De Kauwe, M.G., Keenan, T.F., Medlyn, B.E. and Prentice, I.C.  
645 (2019) Observed and modelled historical trends in the water-use efficiency of plants and ecosystems.  
646 *Global Change Biology*, 25, 2242–2257. doi:10.1111/gcb.14634

647 Li, C., Han, J., Liu, Z., Tu, Z. and Yang, H. (2024) A harmonized global gridded transpiration  
648 product based on collocation analysis. *Scientific Data*, 11, 604. doi:10.1038/s41597-024-03425-7

649 Lian, X., Piao, S., Li, L.Z.X., Li, Y., Huntingford, C., Ciais, P., Cescatti, A., Janssens, I.A.,  
650 Peñuelas, J., Buermann, W., Chen, A., Li, X., Myneni, R.B., Wang, X., Wang, Y., Yang, Y., Zeng,  
651 Z., Zhang, Y. and McVicar, T.R. (2020) Summer soil drying exacerbated by earlier spring greening  
652 of northern vegetation. *Science Advances*, 6, eaax0255. doi:10.1126/sciadv.aax0255

653 Liang, X., Wang, D., Ye, Q., Zhang, J., Liu, M., Liu, H., Yu, K., Wang, Y., Hou, E., Zhong,  
654 B., Xu, L., Lv, T., Peng, S., Lu, H., Sicard, P., Anav, A. and Ellsworth, D.S. (2023) Stomatal

655 responses of terrestrial plants to global change. *Nature Communications*, 14, 2188.  
656 doi:10.1038/s41467-023-37934-7

657 Liu, L., Gudmundsson, L., Hauser, M., Qin, D., Li, S. and Seneviratne, S.I. (2020a) Soil  
658 moisture dominates dryness stress on ecosystem production globally. *Nature Communications*, 11,  
659 4892. doi:10.1038/s41467-020-18631-1

660 Liu, Y., Kumar, M., Katul, G.G., Feng, X. and Konings, A.G. (2020b) Plant hydraulics  
661 accentuates the effect of atmospheric moisture stress on transpiration. *Nature Climate Change*, 10,  
662 691–695. doi:10.1038/s41558-020-0781-5

663 Liu, Y., Lin, Z., Wang, Z., Chen, X., Han, P., Wang, B., Wang, Z., Wen, Z., Shi, H., Zhang, Z.  
664 and Zhang, W. (2023) Discriminating the impacts of vegetation greening and climate change on the  
665 changes in evapotranspiration and transpiration fraction over the Yellow River Basin. *Science of  
666 the Total Environment*, 904, 166926. doi:10.1016/j.scitotenv.2023.166926

667 Liu, Y., Wang, Y., Zhao, Y., Chen, S., Wang, L., Yang, W., Li, X., Li, X., Lei, H., Chang, H.,  
668 Zhai, J., Zhu, Y., Wang, Q. and Ye, T. (2025) Evapotranspiration stress intensifies with enhanced  
669 sensitivity to soil moisture deficits in a rapidly greening China. *Hydrology and Earth System  
670 Sciences*, 29, 3379–3404. doi:10.5194/hess-29-3379-2025

671 Martínez-Vilalta, J. and García-Forner, N. (2017) Water potential regulation, stomatal  
672 behaviour and hydraulic transport under drought: deconstructing the iso/anisohydric concept. *Plant,  
673 Cell & Environment*, 40, 962–976. doi:10.1111/pce.12846

674 McDowell, N.G., Sapes, G., Pivovarov, A., Adams, H.D., Allen, C.D., Anderegg, W.R.L.,  
675 Arend, M., Breshears, D.D., Brodrick, T., Choat, B., Cochard, H., De Cáceres, M., De Kauwe, M.G.,  
676 Grossiord, C., Hammond, W.M., Hartmann, H., Hoch, G., Kahmen, A., Klein, T., Mackay, D.S.,  
677 Mantova, M., Martínez-Vilalta, J., Medlyn, B.E., Mencuccini, M., Nardini, A., Oliveira, R.S., Sala,  
678 A., Tissue, D.T., Torres-Ruiz, J.M., Trowbridge, A.M., Trugman, A.T., Wiley, E. and Xu, C. (2022)  
679 Mechanisms of woody-plant mortality under rising drought, CO<sub>2</sub> and vapour pressure deficit. *Nature  
680 Reviews Earth & Environment*, 3, 294–308. doi:10.1038/s43017-022-00272-1

681 Miralles, D.G., Bonte, O., Koppa, A., Baez-Villanueva, O.M., Tronquo, E., Zhong, F., Beck,  
682 H.E., Hulsman, P., Dorigo, W., Verhoest, N.E.C. and Haghdoost, S. (2025) GLEAM4: global land  
683 evaporation and soil moisture dataset at 0.1° resolution from 1980 to near present. *Scientific Data*,  
684 12, 416. doi:10.1038/s41597-025-04610-y

685 Muñoz-Sabater, J., Dutra, E., Agustí-Panareda, A., Albergel, C., Arduini, G., Balsamo, G.,  
686 Boussetta, S., Choulga, M., Harrigan, S., Hersbach, H., Martens, B., Miralles, D.G., Piles, M.,  
687 Rodríguez-Fernández, N.J., Zsoter, E., Buontempo, C. and Thépaut, J.-N. (2021) ERA5-Land: a  
688 state-of-the-art global reanalysis dataset for land applications. *Earth System Science Data*, 13, 4349–  
689 4383. doi:10.5194/essd-13-4349-2021

690 Niu, Z., He, H., Zhu, G., Ren, X., Zhang, L. and Zhang, K. (2020) A spatial-temporal  
691 continuous dataset of the transpiration to evapotranspiration ratio in China from 1981–2015.  
692 *Scientific Data*, 7, 369. doi:10.1038/s41597-020-00693-x

693 Novick, K.A., Ficklin, D.L., Stoy, P.C., Williams, C.A., Bohrer, G., Oishi, A.C., Papuga, S.A.,  
694 Blanken, P.D., Noormets, A., Sulman, B.N., Scott, R.L., Wang, L. and Phillips, R.P. (2016) The

695 increasing importance of atmospheric demand for ecosystem water and carbon fluxes. *Nature*  
696 *Climate Change*, 6, 1023–1027. doi:10.1038/nclimate3114

697 Novick, K.A., Ficklin, D.L., Grossiord, C., Konings, A.G., Martínez-Vilalta, J., Sadok, W.,  
698 Trugman, A.T., Williams, A.P., Wright, A.J., Abatzoglou, J.T., Dannenberg, M.P., Gentine, P.,  
699 Guan, K., Johnston, M.R., Lowman, L.E.L., Moore, D.J.P. and McDowell, N.G. (2024) The impacts  
700 of rising vapour pressure deficit in natural and managed ecosystems. *Plant, Cell & Environment*, 47,  
701 3561–3589. doi:10.1111/pce.14846

702 Qing, Y., Wang, S., Ancell, B.C. and Yang, Z.-L. (2022) Accelerating flash droughts induced  
703 by the joint influence of soil moisture depletion and atmospheric aridity. *Nature Communications*,  
704 13, 1139. doi:10.1038/s41467-022-28752-4

705 Schlesinger, W.H. and Jasechko, S. (2014) Transpiration in the global water cycle. *Agricultural*  
706 *and Forest Meteorology*, 189–190, 115–117. doi:10.1016/j.agrformet.2014.01.011

707 Song, J., Zhou, S., Yu, B., Li, Y., Liu, Y., Yao, Y., Wang, S. and Fu, B. (2024) Serious  
708 underestimation of reduced carbon uptake due to vegetation compound droughts. *npj Climate and*  
709 *Atmospheric Science*, 7, 23. doi:10.1038/s41612-024-00571-y

710 Stoy, P.C., El-Madany, T.S., Fisher, J.B., Gentine, P., Gerken, T., Good, S.P., Klosterhalfen,  
711 A., Liu, S., Miralles, D.G., Perez-Priego, O., Rigden, A.J., Skaggs, T.H., Wohlfahrt, G., Anderson,  
712 R.G., Coenders-Gerrits, A.M.J., Jung, M., Maes, W.H., Mammarella, I., Mauder, M., Migliavacca,  
713 M., Nelson, J.A., Poyatos, R., Reichstein, M., Scott, R.L. and Wolf, S. (2019) Reviews and  
714 syntheses: turning the challenges of partitioning ecosystem evaporation and transpiration into  
715 opportunities. *Biogeosciences*, 16, 3747–3775. doi:10.5194/bg-16-3747-2019

716 Sun, S., Liu, Y., Chen, H., Ju, W., Xu, C.-Y., Liu, Y., Zhou, B., Zhou, Y., Zhou, Y. and Yu,  
717 M. (2022) Causes for the increases in both evapotranspiration and water yield over vegetated  
718 mainland China during the last two decades. *Agricultural and Forest Meteorology*, 324, 109118.  
719 doi:10.1016/j.agrformet.2022.109118

720 Wang, J. (2026) Global daily 1 km gapless XCO<sub>2</sub> (2003–2023) derived from multi-satellite  
721 observations and a spatiotemporal deep learning framework. *Environmental Impact Assessment*  
722 *Review*, 117, 108146. doi:10.1016/j.eiar.2025.108146

723 Wei, Z., Yoshimura, K., Wang, L., Miralles, D.G., Jasechko, S. and Lee, X. (2017) Revisiting  
724 the contribution of transpiration to global terrestrial evapotranspiration. *Geophysical Research*  
725 *Letters*, 44, 2792–2801. doi:10.1002/2016GL072235

726 Xia, J., Xia, X., Chen, Y., Shen, R., Zhang, Z., Liang, B., Wang, J. and Yuan, W. (2023)  
727 Reconstructing long-term forest age of China by combining forest inventories, satellite-based forest  
728 age and forest cover data sets. *Journal of Geophysical Research: Biogeosciences*, 128,  
729 e2023JG007492. doi:10.1029/2023JG007492

730 Xu, H., Yue, C., Zhang, Y., Liu, D. and Piao, S. (2023) Forestation at the right time with the  
731 right species can generate persistent carbon benefits in China. *Proceedings of the National Academy*  
732 *of Sciences of the United States of America*, 120, e2304988120. doi:10.1073/pnas.2304988120

733 Yuan, W., Zheng, Y., Piao, S., Ciais, P., Lombardozzi, D., Wang, Y., Ryu, Y., Chen, G., Dong,  
734 W., Hu, Z., Jain, A.K., Jiang, C., Kato, E., Li, S., Lienert, S., Liu, S., Nabel, J.E.M.S., Qin, Z., Quine,  
735 T., Sitch, S., Smith, W.K., Wang, F., Wu, C., Xiao, Z. and Yang, S. (2019) Increased atmospheric

736 vapor pressure deficit reduces global vegetation growth. *Science Advances*, 5, eaax1396.  
737 doi:10.1126/sciadv.aax1396

738 Zahra, N., Hafeez, M.B., Kausar, A., Al Zeidi, M., Asekova, S., Siddique, K.H.M. and Farooq,  
739 M. (2023) Plant photosynthetic responses under drought stress: effects and management. *Journal of*  
740 *Agronomy and Crop Science*, 209, 651–672. doi:10.1111/jac.12652

741 Zhang, K., Chen, H., Ma, N., Shang, S., Wang, Y., Xu, Q. and Zhu, G. (2024) A global dataset  
742 of terrestrial evapotranspiration and soil moisture dynamics from 1982 to 2020. *Scientific Data*, 11,  
743 445. doi:10.1038/s41597-024-03271-7

744 Zhou, S., Zhang, Y., Williams, A.P. and Gentile, P. (2019) Projected increases in intensity,  
745 frequency, and terrestrial carbon costs of compound drought and aridity events. *Science Advances*,  
746 5, eaau5740. doi:10.1126/sciadv.aau5740

747